Flow reversals during upwelling conditions on the New Jersey inner shelf

Robert J. Chant, Scott Glenn, and Josh Kohut

Institute of Marine and Coastal Science, Rutgers University, New Brunswick, New Jersey, USA

Received 30 April 2003; revised 15 June 2004; accepted 22 July 2004; published 13 November 2004.

[1] The temporal evolution of a flow reversal during upwelling conditions along New Jersey's inner shelf is characterized with shipboard, moored, and remote observations. The flow reversal occurs nearshore in the form of a subsurface jet with maximum velocities exceeding 30 cm/s. The jet is most intense in the thermocline, commences during maximum alongshore wind stress, and has a spin-up time approximately equal to the local inertial period. The jet also has a surface signature apparent in ocean current radar data that shows the jet veering offshore and feeding an upwelling center that drifts southward at 5 cm/s. Moored instrumentation within the upwelling center indicates that cross-shelf transport in the warm surface layer is consistent with the predicted Ekman transport prior to the spin-up of the jet, but exceeds Ekman transport thereafter. However, onshore transport in the lower layer never compensates for offshore flow in the surface layer, suggestive that the mass balance requires a three-dimensional closure. Finally, we suggest that the flow reversal provides a significant fraction of cool water to the evolving upwelling center, and that the offshore veering is due to enhanced friction over a shoaling and rougher topography. *INDEX TERMS:* 4279 Oceanography: General: Upwelling and convergences; 4524 Oceanography: Physical: Fine structure and microstructure; 4520 Oceanography: Physical: Eddies and mesoscale processes; *KEYWORDS:* upwelling, flow reversal, Ekman Transport Index

Citation: Chant, R. J., S. Glenn, and J. Kohut (2004), Flow reversals during upwelling conditions on the New Jersey inner shelf, *J. Geophys. Res.*, *109*, C12S03, doi:10.1029/2003JC001941.

1. Introduction

[2] The most simplistic model of coastal upwelling, based on Ekman dynamics, consists of an offshore transport of warm surface water that is compensated by an onshore transport of cold fluid in the bottom layer. The transport of fluid in the surface layer is the Ekman transport, $\tau/\rho f$, where τ, ρ, and f are the alongshore wind stress, density, and the Coriolis frequency, respectively. Numerous theoretical and experimental studies have been motivated by this simple two-dimensional model, and the results have produced a more sophisticated view of coastal circulation processes. *Huyer* [1983] described an alongshore downwind baroclinic surface jet that is in thermal wind balance with the tilted isopycnals of an upwelling front. *Lentz and Trowbridge* [1991], *Trowbridge and Lentz* [1991], and *MacCready and Rhines* [1993] have invoked the combined effects of baroclinicity and Ekman dynamics over a sloping bottom to characterize the arrested Ekman layer and the resulting asymmetries in coastal circulation in response to upwelling and downwelling wind forcing. Recently, *Austin and Barth* [2002] have characterized the time-dependent nature of upwelling based on a series of high-resolution cross-shelf temperature sections.

[3] Although many aspects of coastal upwelling are captured by these two-dimensional models [*Winant et al.*, 1987; *Wang*, 1997; *Chen and Wang*, 1990], many observations clearly indicate that upwelling processes are often three-dimensional. Perhaps the most cited example is a summary by *Smith* [1981], who notes that while observations of wind-driven offshore transport in the upper layer off the American west and African coasts are consistent with Ekman's theory, the onshore transport at depth is not, and that this implies a divergence/convergence in the alongshore currents. Three-dimensional structure is also suggested in satellite-derived sea surface temperature imagery that emphasizes a rich alongshore structure characterized by offshore squirts and upwelling centers [*Bernstein et al.*, 1977; *Traganza et al.*, 1981; *Glenn et al.*, 1996]. Alongshore variability may be triggered by coastal promontories [*Kosro*, 1987] and the underlying bathymetry [*Glenn et al.*, 1996; *Song et al.*, 2001] as well as internal dynamics alone that can drive instabilities and produce coherent alongshore structure [*Barth*, 1994].

[4] While the classic textbook upwelling model highlights the cross-shelf flows, currents are predominately in the alongshore direction. This is particularly true in the nearshore where currents are highly polarized and aligned in the alongshore direction [*Kosro*, 1987]. This polarization makes estimates of the cross-shelf flows sensitive to the definition of the along-shelf direction. Nevertheless, while synoptic current maps show a complex flow field that rarely resembles the conceptual model, many of the idealized features do appear in the averaged fields [*Kosro*, 1987; *Winant et al.*, 1987; *Munchow and Chant*, 2000].

0148-0227/04/2003JC001941$09.00

[5] *Munchow and Chant* [2000] provide a statistical description of wind-driven flows on New Jersey's inner shelf during the summer months when mean winds are upwelling favorable (to the north). During this period the mean currents have an appreciable offshore component in the surface with a weaker and noncompensating onshore transport at depth. Alongshore mean flows contain a downwind surface jet, similar to the thermal wind jet described by *Huyer* [1983] and *Kosro* [1987], and a subsurface flow in the opposite direction that is strongest near the coast. Flow reversals at depth have also been reported to occur along the U.S. west coast [*Winant et al.*, 1987; *Kosro*, 1987; *Huyer*, 1983]. *Kosro* [1987] indicates that this return flow can surface near the coast. Model hindcasts of the CODE observations indicate that the return flow is driven by an alongshore pressure gradient [*Chen and Wang*, 1990]. Flow reversals also occur as upwelling winds relax [*Wang*, 1997] or during times of appreciable wind stress curl [*Wang*, 1997]. These nearshore flow reversals occurred frequently during CODE and contributed significantly to the heat budget and emphasize that upwelling can be a fully three-dimensional process [*Send et al.*, 1987]. Of particular relevance to observations presented in this paper are results from numerical simulations by *Gan and Allen* [2002a, 2002b], who elucidate the dynamics of topographically driven flow reversal when upwelling winds relax. Specifically, they demonstrate that the flow reversals are driven by an adverse pressure gradient that develops downstream of coastal promontories.

[6] Many of these processes are evident in data collected during upwelling conditions along New Jersey's inner shelf. In particular, the development of a flow reversal during upwelling conditions appear to impact the development of a recurrent upwelling center in the vicinity of Rutgers University's Long-term Ecosystem Observatory (LEO) located on New Jersey's inner shelf (Figure 1). Note that the flow reversal discussed in this paper occurs during upwelling conditions in contrast to the aforementioned west-coast studies where flow reversals are often reported to occur during relaxation. The evolution of the flow reversal described in this paper is based on data collected from shipboard, moored, and remote platforms in July of 1998. This event typifies numerous upwelling events that have been observed along the New Jersey shelf over the last decade [*Glenn et al.*, 1996; *Munchow and Chant*, 2000; *Song et al.*, 2001]. For example, the temporal and spatial evolution of the event is similar to EOF analysis presented by *Munchow and Chant* [2000] where the phasing between mode 1 and mode 2 time series reveals a cyclonic rotating eddy with inshore flow reversals as upwelling winds relax. This structure is also apparent in the theoretical study by *Song et al.* [2001], a study motivated by the interaction between upwelling circulation and topographic variability on the New Jersey shelf. They revealed that topography enhances onshore transport of cold bottom fluid in the bottom Ekman layer downwind of topographic highs while reducing lower layer transport upwind of a high. This along-shelf structure was characterized in terms of a topographic perturbation velocity in the bottom Ekman layer that, like in our observations, contains a flow reversal at the coast.

[7] The New Jersey shelf becomes strongly thermally stratified during the summer months when surface to bottom temperature differences can exceed 15°C in 20 m of water. The stratification is characterized by a two-layer system separated by a sharp thermocline, generally less than 5 m in thickness. Upwelling occurs during the summer months in response to the prevailing summertime southwesterly winds driven by the Bermuda High. The cool upwelled water is supplied by the shoreward side of New York Bight's cold pool within which minimum summertime bottom temperatures off the New Jersey coast occur on the mid-shelf in the late summer due to advective processes [*Houghton et al.*, 1982]. In contrast, surface water temperature reaches a maximum during July. The combination of the supply of cold water to the cold pool and surface heating maintains strong stratification throughout the summer months.

[8] The data on which this paper is based were collected as part of an interdisciplinary study to investigate interactions between wind-driven circulation and primary production. The field program was conducted in July 1998 in the vicinity of LEO. LEO is located in one of three recurring upwelling centers that develop along the New Jersey coast in response to summertime southerly winds [*Glenn et al.*, 1996]. These upwelling centers occur to the north of topographic highs that are remnant river deltas. Topographic contours in Figure 1 contain one of these highs along the C-line and show that the high is associated with increased roughness. The rougher topography is due to larger ridge and swale features that are evident in the southern half of the figure.

2. Field Experiment

[9] The 1998 field experiment characterized the evolving three-dimensional structure of a coastal upwelling event. It was comprised of two ADCP moorings (Figure 1), a thermistor string, multiple shipboard ADCP/CTD sections that focused on two cross-shore sections, sea surface temperature from AVHRR imagery, and surface currents fields from a land-based CODAR system [*Kohut and Glenn*, 2003]. The offshore mooring was in 23 m of water. Velocity measurement spanned from 1.6 m above bottom to 20.6 mab (2.4 m below the surface) at a vertical resolution of 1 m. The inshore mooring was in 12 m of water with vertical resolution of 1 m from 1.6 mab to 10.6 mab (1.4 m below surface). The thermistor string at the offshore moorings contained a thermistor every 50 cm from 1.5 m below the surface to 19 m below the surface.

[10] Shipboard instrumentation included a 1200-kHz broadband RDI-ADCP towed abeam of the ship. The ADCP was operated in mode 1 and collected single ping data in 1-m bins. Astern of the ship we towed a Guildline minibat equipped with a CTD and fluorometer. Data from the minibat were screened to include only downcasts providing a horizontal resolution of 200–400 m. ADCP data were screened for excessive acceleration and averaged into 2-min ensembles, which, at our typical ship speed of 3 m/s, represents a 200-m footprint. Meteorological data were taken from the NOAA buoy off Delaware Bay, approximately 100 km from the site.

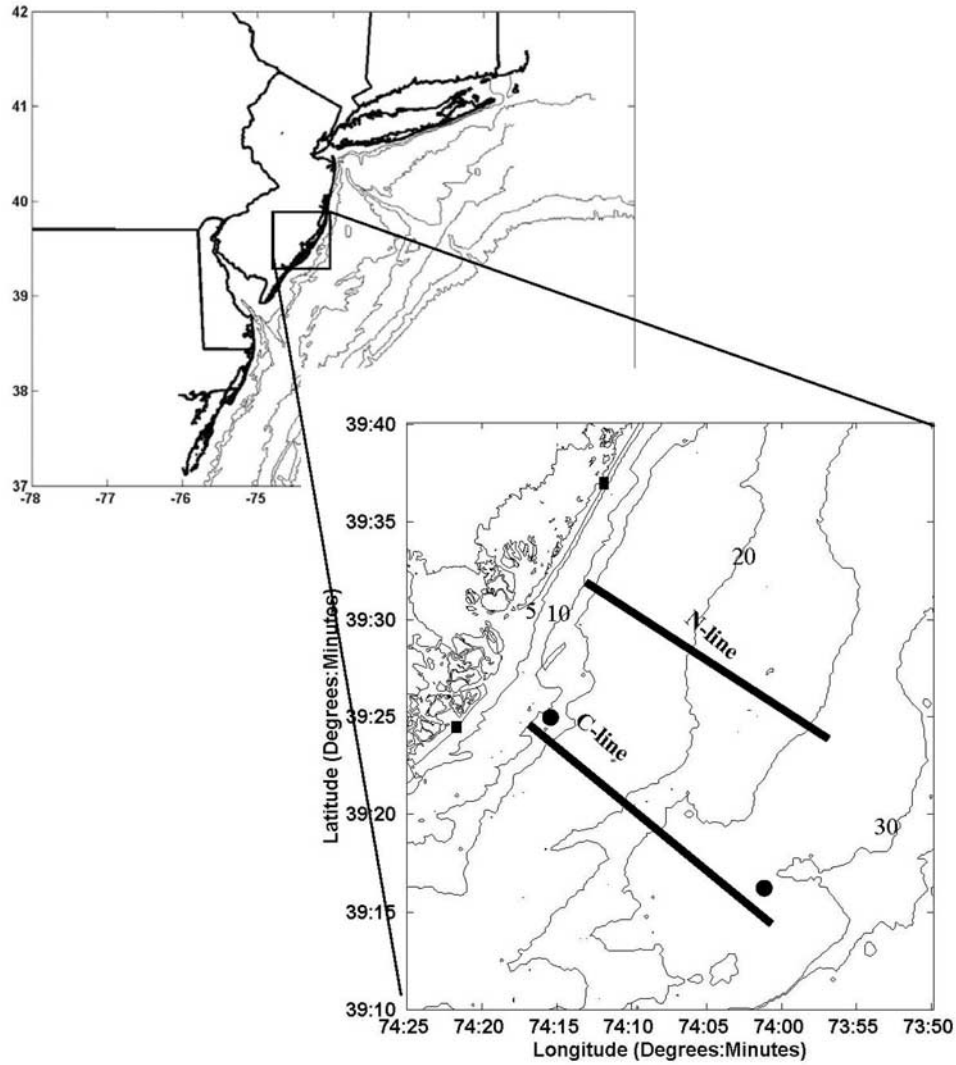

Figure 1. Study area. Shipboard transects are depicted by thick lines on lower map. Current meter locations are depicted as solid circles. LEO-15 is the inshore circle. Solid black squares depict the CODAR sites. Isobaths in the large-scale map are 15, 20, 40, 60, 80, 100, and 200 m. Isobaths in small-scale figure are in increments of 5 m.

[11] Time series of currents from the moorings and CODAR unit have been low-pass filtered with a cutoff period of 32 hours to remove tidal and inertial period motion. Tidal motion was removed from the towed ADCP data by a tidal model described below. Note that the detided shipboard ADCP data still contain tidal period motion not included in the tidal model, such as intermittent internal tides, and near-inertial motion. Inertial motion has been shown to at times dominate currents during upwelling periods at this location [*Chant*, 2001], but because our shipboard survey repeated sections 2–3 times inside of a tidal cycle, we can assess to what extent the results are aliased by tidal period motion not included in the tidal model.

[12] The coordinate system used in this paper defines x and y as the offshore and up-shelf directions, while u and v represent offshore and up-shelf flow. Up-shelf is defined to the north, opposite to the direction of Kelvin wave propagation.

3. Tidal Model

[13] The depth-averaged shipboard ADCP data collected in July 1998 and July 1999 were fit to the M_2 tidal constituent with a *Candela et al.* [1992] type method using a second-order polynomial for the cross-shore structure of the alongshore and cross-shore M_2 tidal motion along lines C and N (Figure 2). To include the spring/neap modulation of amplitude and phase of the semidiurnal motion, we used a method similar to that described by *Signell and Geyer* [1991] whereby the horizontal structure of the tidal motion is determined by the shipboard data, and this horizontal structure is temporally modulated by spring/neap variability from a nearby fixed point time series. In our

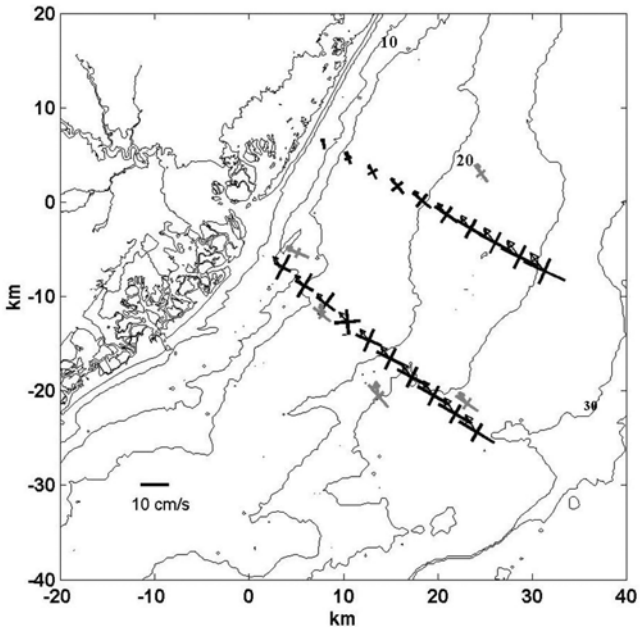

Figure 2. Depth-averaged semidiurnal tidal ellipses. Black ellipses are obtained from shipboard surveys. Shaded ellipses were obtained from moored instruments. Moorings from 1998 are the two just north of the C-line. Other moorings are from 1996. Arrows indicate the phase of the tide. Depth contours are in increments of 5 m.

case we used the depth-averaged current from the offshore mooring to modulate the amplitude and phase of the M_2 tidal constituent obtained from the shipboard data. Specifically, the amplitude of the tidal motion was modulated by $A(t)/A_{M2}$ where $A(t)$ is the amplitude of the time series demodulated at the M_2 frequency and A_{M2} is the least squares estimate of the depth-averaged M_2 tidal motion at the mooring. Similarly, the phase of the M_2 tide is modulated by the difference between the phase of the demodulated time series and the phase of the M_2 tidal constituent at the mooring ($\Delta\theta = \theta_{dmd} - \theta_{M2}$). Thus for the depth-averaged cross-shore motion the tidal motion is

$$U = \frac{A_{dmd}}{A_{M2}} \times A_i(x) \times \cos(\omega t + \theta_i(x) - \Delta\theta(t)), \qquad (1)$$

where $A_i(x)$ and $\theta_i(x)$ are obtained from the second-order polynomial fit of the shipboard data, and the index i represents the fit along the C-line ($i = 1$) and N-line ($i = 2$). The alongshore semidiurnal motion is calculated in an identical fashion.

[14] The vertical structure of the tidal motion was determined with the offshore mooring as follows. The depth was transformed to a sigma coordinate system, and the depth-dependent tidal motion was characterized by the ratio of the depth-dependent M_2 tidal amplitude to the depth-averaged M_2 tidal amplitude (Figure 3, left panel) and the difference in phase between the depth-dependent and depth-averaged motion (Figure 3, right panel). The final step in the tidal model is to multiply the depth-averaged tidal model (1) by the depth-dependent structure to get the depth-dependent amplitude of the tidal motion. Similarly, the phase of the depth-averaged motion is shifted by the vertical phase structure as in shown in Figure 3 (right panel).

[15] The leakage of the along-shelf flows into estimates of diurnal tidal motion made with the shipboard data was severe and likely due the fact that shipboard surveys were only 12 hours and do not cover the entire diurnal period. However, moored data from 1998 and 1996 indicate that there is little cross-shelf structure to the diurnal motion (Figure 4), and subsequently, diurnal motion in the tidal model is estimated by a least squares fit to the moored data. The modeled diurnal tide is based on data collected between days 190 and 210 from the offshore mooring. Thus the diurnal tidal model has a vertical structure, but no horizontal variability.

4. Results

4.1. Forcing

[16] We focus on a single upwelling event that occurred between July 20 and July 25 (days 201–206) in response to a 4- to 5-day period of upwelling-favorable winds (Figure 5). On the basis of winds from the NOAA buoy off Delaware Bay, we estimate the alongshore wind stress, τ_{s_y}, with a quadratic formulation $\tau_{s_y} = \rho_a C_d W_a |W|$, where W_a is the alongshore wind speed, $|W|$ is the wind's magnitude, ρ_a is the density of air (1.2 kg/m^3), and $C_d = 1.2 \times 10^{-3}$ [*Large and Pond*, 1981]. The alongshore direction is defined by the orientation of the coastline (taken to be 34° east of north). The maximum alongshore wind stress of 0.7 dynes/cm^2 occurred during day 200. Weak wind reversals occur on days 205–206 followed by weak upwelling-favorable winds up to day 210.

4.2. Surface Signature

[17] The response of this shallow, stratified shelf to the wind is rapid. On 21 July (day 202), 1 day after the

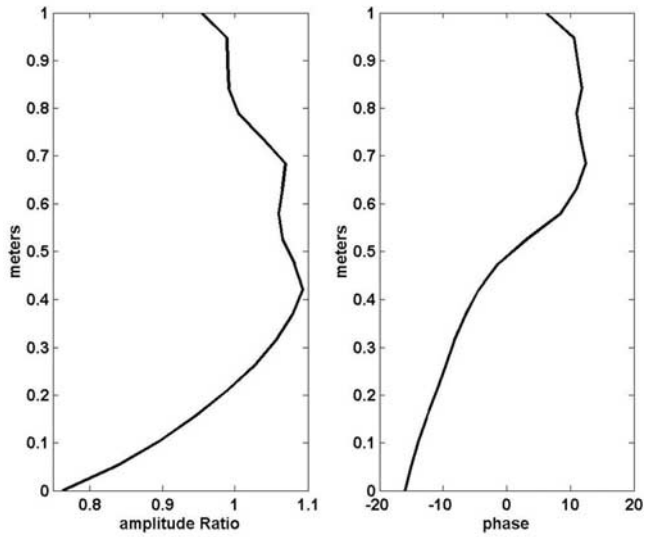

Figure 3. (top) Vertical structure of the ratio of the major axis of the depth dependent M_2 tidal constituent to the major axis of the depth averaged M_2 tidal motion from the offshore mooring. (bottom) Vertical phase structure of the M_2 tide used in the tidal model defined as the difference between the depth-dependent and depth-averaged phase.

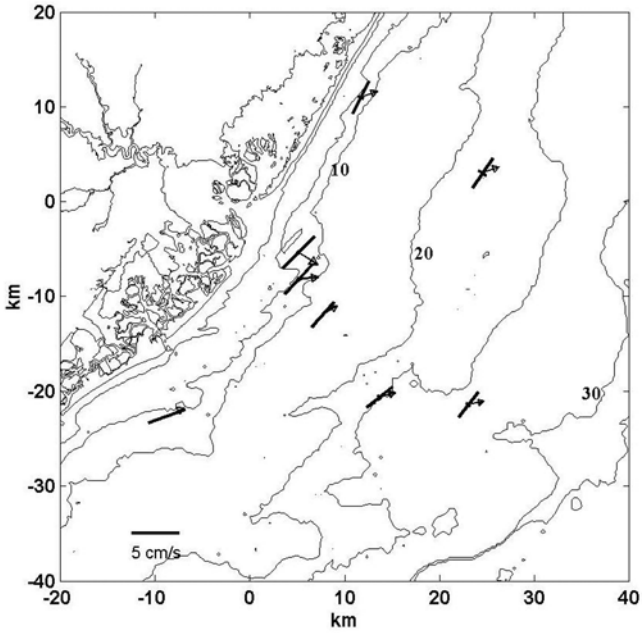

Figure 4. Depth-averaged diurnal tidal ellipses from moored data. Arrows indicate the phase of the tide. Depth contours are in increments of 5 m.

commencement of upwelling-favorable winds, AVHRR imagery indicates that cool water has surfaced at the coast and extends offshore just to the north of LEO (Figure 6). By 23 July the offshore extension of upwelled water has moved to the south, despite continued upwelling-favorable winds. On both days, low-passed CODAR data reveal cyclonically rotating surface current fields. On 21 July the center of recirculation is at 39°30′N, 74°05′W. On 23 July (day 203) the feature has migrated to the south into the full view of the CODAR footprint with the center of recirculation located at 39°25′N, 74°05′. Between these two images the center of recirculation has moved approximately 9 km in 45 hours, corresponding to an average speed of 5 cm/s. Both images reveal a strong nearshore upwind southerly flow of cool water that turns offshore over the rougher topography at the inshore side of the C-line. Unfortunately the CODAR unit was down due to a power outage during the onset of upwelling (18–19 July), so we are unable to depict the flow structure prior to the development of the nearshore jet.

[18] During the commencement of this upwelling event and subsequent spin-up of the nearshore-upwind jet, we conducted numerous cross-shelf surveys along the N and C lines. On the basis of these sections, we describe in detail the spin-up of the nearshore upwind jet.

4.3. Upwind Jet

[19] Cross-shelf sections of detided along-shelf currents and temperature obtained on 23 and 24 July are presented in Figure 7. Both figures show a nearshore subsurface jet that flows down-shelf with maximum flow speeds exceeding 30 cm/s. The highest velocities in the jet occur at approximately the 18°C isotherm. Isotherms in the jet are spread, suggestive of enhanced mixing in the jet or of a convergence of fluid in the thermocline. Offshore, the flow is to the north where up-shelf currents exceed 25 cm/s. The offshore jet is situated just seaward of upward sloping isotherms, and the sign and magnitude of the vertical shear is consistent with a thermal wind balance. Estimates of the terms $f\frac{\partial v}{\partial z}$ and $\frac{g\partial \rho}{\rho \partial x}$ from the 23 July section indicates that both are both approximately 5×10^{-6} s^{-2}, suggesting that the vertical shear is in near-thermal balance. A sharp thermocline 3–5 m thick separates these warm surface waters from a cold bottom mixed layer where temperatures are below 12°C. The flow reversal is not associated with a buoyant coastal current associated with fresh water flows from the Hudson River, as described by *Yankovsky et al.* [2000]. The salinity field (not shown) is characterized by a low saline lower layer (31.5 psu) and a fresh upper layer (30. 5 psu) that is associated with shelf-wide two-layer structure rather than a coastal buoyant current.

[20] From the cross-shelf shipboard sections the volume of down-shelf transport is estimated (Figure 8) as $\int_{Z_t}^{Z_b}\int_{X_1}^{X_2} \min(v_{\mathrm{dt}}, 0)\, \partial x \partial z$, where Z_t and Z_b are the top and bottom ADCP bin, X_1 and X_2 are distances from shore of the inshore and offshore sides of the section, and v_{dt} is the detided along-shelf flow and is defined as negative for down-shelf flow. Prior to day 201, sampling occurred only on the C-line, during which time down-shelf flows are weak. Up-shelf flows of approximately 20,000 m^3/s are observed on both 16 and 17 July (not shown). On 20 July (day 201) we sampled the C-line once and the N-line twice. On all three transects the down-shelf transport is again weak. Up-shelf transport along the N-line is slightly less than 20,000 m^3/s, while it exceeds 30,000 m^3/s along the C-line (not shown). The spin-up of the jet occurs between days 201 and 202. On 21 July (day 202) the N-line was completed three times, from which three consistent estimates of down-shelf transport of ~30,000 m^3/s were made. The onset of down-shelf

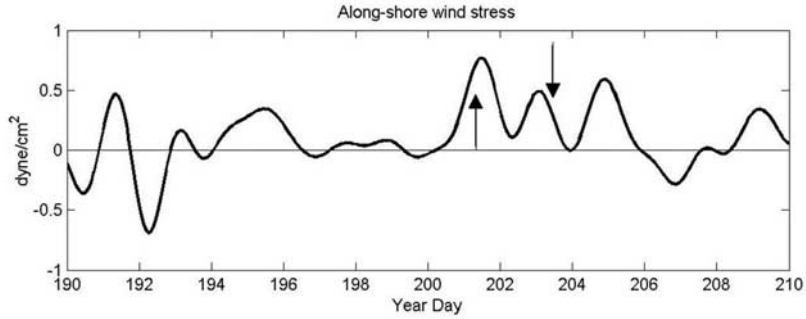

Figure 5. Alongshore wind stress. Arrows indicate times of current maps shown in Figure 6.

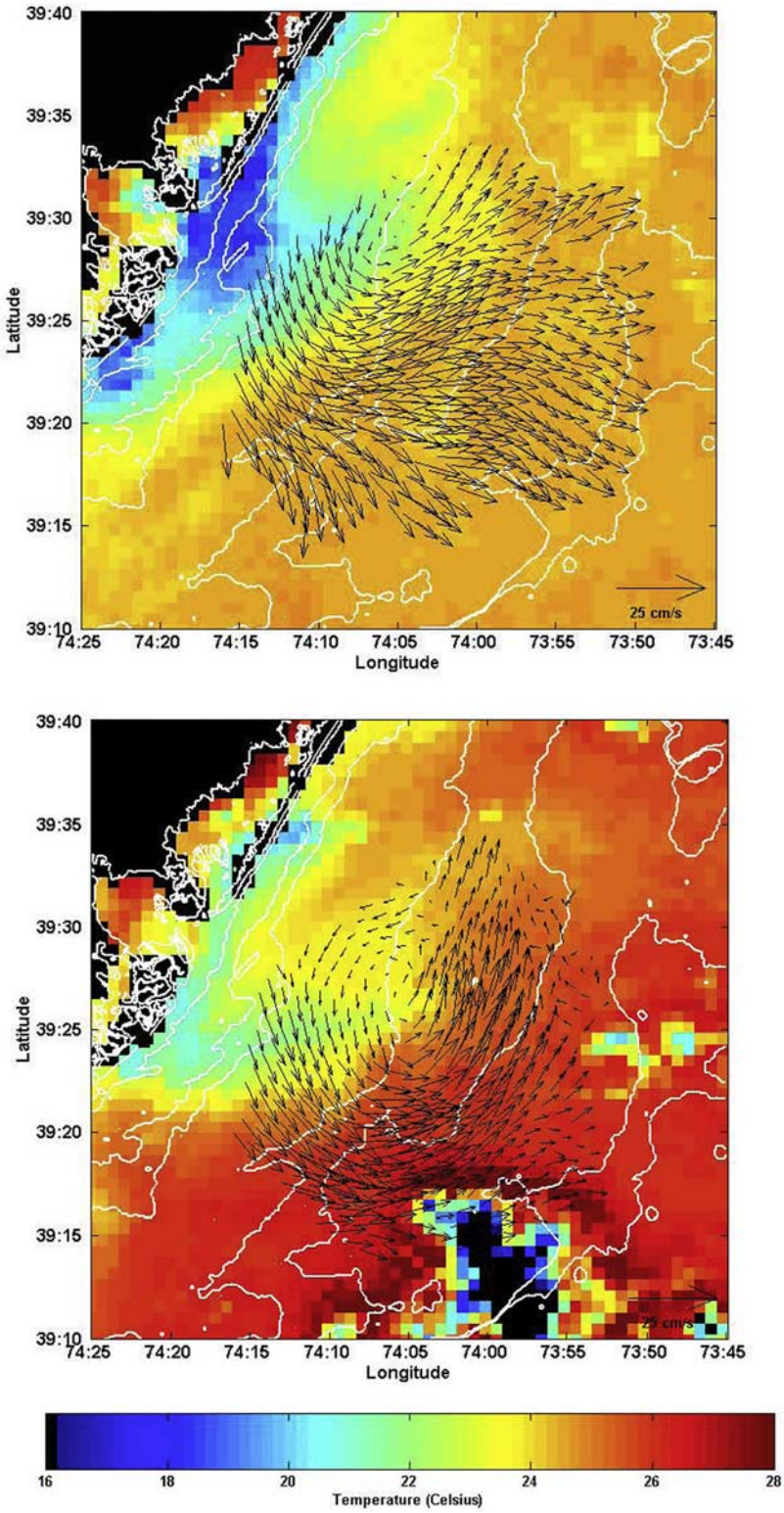

Figure 6. Overlay of sea-surface temperature from AVHRR and low-passed surface currents from CODAR for (top) 21 July 0820 GMT and (bottom) 23 July 1135 GMT.

transport coincides with the maximum along-shelf wind stress, and the spin-up time of the jet is on the order of an inertial period. This temporal evolution is depicted by the curve $Q = 35{,}000 \times (e^{-t/T} - 1)$ in Figure 8 (bottom panel), where T is the local inertial period (18.8 hours), and emphasizes that the spin-up of the jet occurs at the local inertial period. On subsequent days the upwind transport remains high, averaging nearly 35,000 m^3/s. The fact that

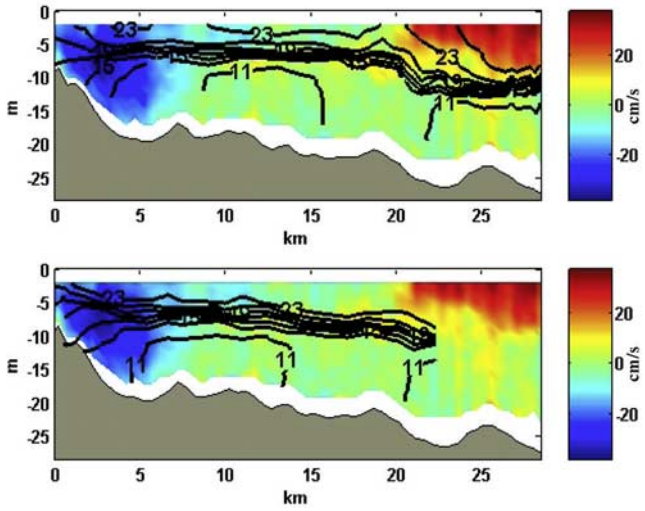

Figure 7. Detided along-shelf current speed and temperature from transects run along the N-line on (top) 23 July 1998 and (bottom) 24 July 1998.

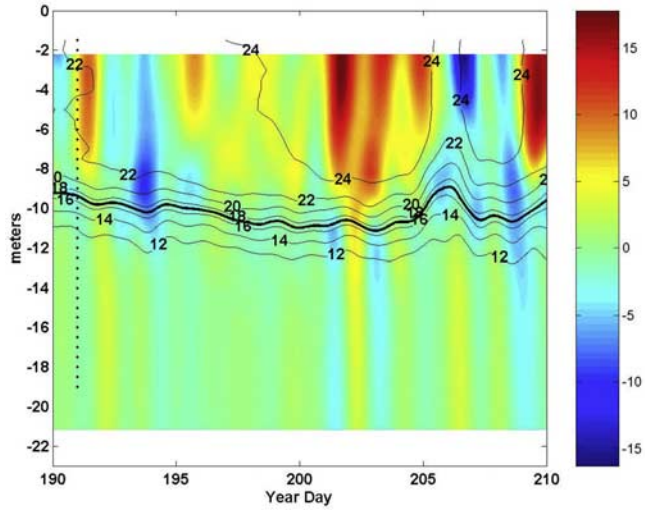

Figure 9. Low-passed temperature from a thermistor chain from the offshore mooring (contours) and low-passed cross-shelf current speed (colors). Positive current is directed offshore. Thick contour line depicts the 17° isotherm that is used to define the interface between the upper and lower layers. Black dots indicate position of thermistors.

transport estimates between repeat sections are fairly consistent indicates that these results are not significantly impacted by tidal period motion that remains in our estimates of the ''detided'' along-shelf flow.

4.4. Moored Data

[21] The thermal structure at the offshore mooring during the entire upwelling event can be characterized as a two-layer system (Figure 9), where a surface mixed layer with temperatures exceeding 22°C is separated from the cold lower layer with temperatures below 11°C, by a thermocline 3–4 m thick. Low-passed cross-shore flows (colors in Figure 9) depict the strong offshore flow in the surface layer following the onset of upwelling-favorable winds toward the end of day 200. Cross-shore flows are significantly weaker in the lower layer and oscillate with the wind variability. Selecting the 17°C isotherm as the interface (thick contour line in Figure 9) we calculated the low-passed along-shelf and cross-shelf transport per unit width (m^2/s) in each layer and plot the result along with the alongshore wind stress in Figure 10 (the alongshore direc-

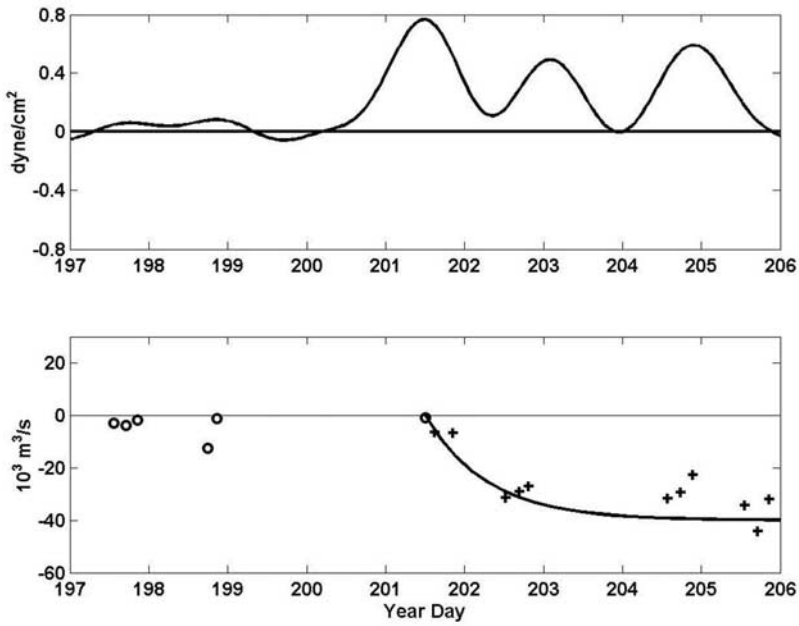

Figure 8. (top) Along-shelf wind stress (reproduction of Figure 4). (bottom) Down-shelf transport from detided shipboard ADCP sections. Circles are estimates made along the C-line; crosses are estimates made along the N-line.

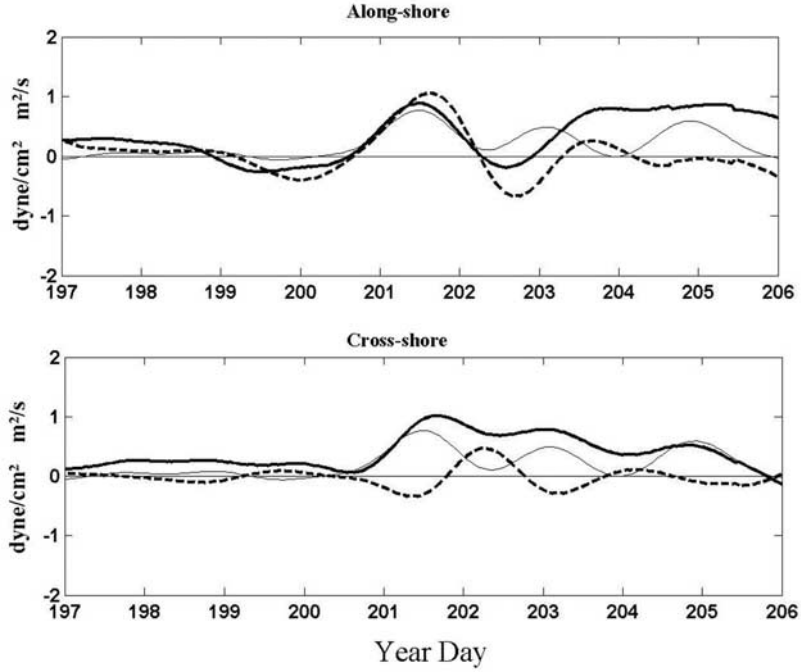

Figure 10. Upper and lower layer flow from the offshore mooring. (top) Along-shelf volume transport per unit width (thick solid line), lower layer (dashed line), and alongshore wind stress (thin solid line). (bottom) Cross-shelf volume transport per unit width in upper layer (thick solid line), lower layer (dashed line), and along-shelf wind stress (thin solid line).

tion for the current, as with the wind, is defined as 34° east of north). Note that these estimates are probably low by 20% due to the near-bottom and near-surface blanking regions. The initial pulse of along-shelf flow in the upper layer on day 201 occurs in phase with the along-shelf wind stress. In the lower layer, along-shelf current response lags the wind forcing. Following this pulse of wind, however, along-shelf currents do not follow the wind forcing, yet upper and lower layers tend to oscillate in a similar fashion, with the lower layer lagging the upper layer. In the cross-shelf direction (bottom panel in Figure 10) the surface layer begins to flow offshore as up-shelf wind accelerates on day 200. Offshore transport in the surface layer peaks shortly after a maximum in along-shelf wind stress. The offshore transport also modulates weakly in phase with the time-varying alongshore wind stress. Weak on-shelf transport is evident in the lower layer, but does not compensate the offshore transport in the surface. Furthermore, the cross-shelf oscillations in the lower layer are more pronounced than those in the upper layer. Cross-shore flow oscillations in the lower layer occur 180° out of phase with those in the surface layer. This is in contrast to oscillations in the alongshore flow where upper and lower layers fluctuations occur with only a small phase difference.

[22] The bottom panel in Figure 11 presents the time integral of the cross-shore transport in the upper and lower layer along with the time integral of $\tau_{sy}/\rho f$, which represents the cross-shore volume of fluid that Ekman dynamics would predict. To include the transport omitted in the near-surface and near-bottom blanking intervals, the layer transports shown in Figure 10 were increased by 20%. During the first day of upwelling-favorable winds, offshore transport in the upper layer is consistent with that predicted by Ekman's theory: The thick and thin solid lines overlap. However, after day 201, offshore flow in the surface layer exceeds that predicted by Ekman's theory, and this timing coincides with initiation of the jet. We suggest that the increased transport in the surface layer is associated with the convergence of upwelled water driven by the flow reversal as it impinges on the shoaling and rougher topography to the south.

[23] At the inshore mooring the alongshore flow in the surface layer is initially to the north but begins to accelerate to the south after day 201 (Figure 12), coinciding with the jet's spin-up. The time lag between the appearance of the jet across N-line and fully developed southward flow at the inshore mooring is consistent with advective speeds of 5–10 cm/s. This speed is more consistent with the speed at which the eddy drifts southward, based on the CODAR imagery, than the observed currents in the jet, which exceed 30 cm/s.

[24] The cross-shore transport in the surface layer at the LEO ADCP is considerably weaker than at the offshore mooring (Figure 12). Furthermore, cross-shore flows here are directed offshore throughout the water column. This is in contrast to the offshore mooring where surface and bottom mean cross-shore flows are in opposite directions. The spatial structure of the mean cross-shore flow during the upwelling event is depicted in Figure 13 along with the cross-shelf transport predicted by Ekman theory (arrow above sea surface). At the offshore mooring the cross-shelf transport at the surface exceeds that predicted by Ekman's theory. At neither the inshore or offshore mooring, however, does the flow in the bottom layer compensate for the offshore flow in the upper layer, and consequently, at both

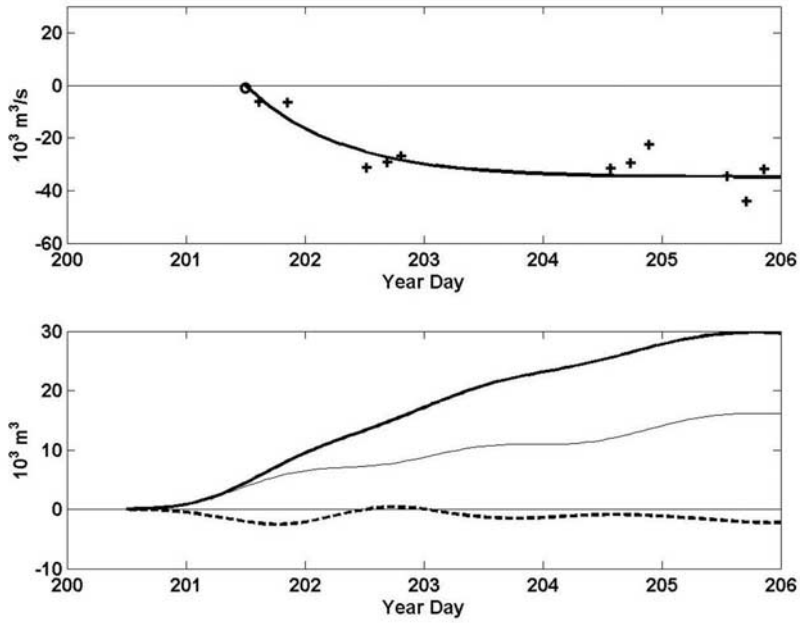

Figure 11. (top) Reproduction of Figure 9 but only plotting days 200–206. (bottom) Time integral of the cross-shelf transport in the upper layer (thick solid line) and lower layer (dashed line), and that predicted by Ekman's theory (thin solid line).

moorings, there is a significant time-mean depth-averaged offshore flow. The basic result does not change for defining the along-shelf direction based on the 10- to 20-km-scale topographic variability. This offshore flow must be maintained by a divergence in the alongshore flow. This divergence is a result of the trajectory of the jet that flows down-shelf along the N-line and veers offshore in the vicinity of LEO. The mean cross-shelf flow from the two moorings indicate that the divergence in the upper layer is equal to the convergence in the lower layer, yet it corresponds to an upwelling velocity of approximately 1 m per day, significantly slower than what is required to drive the rapid upwelling response apparent in the AVHRR imagery. Rather, we suggest that much of the cool water in the

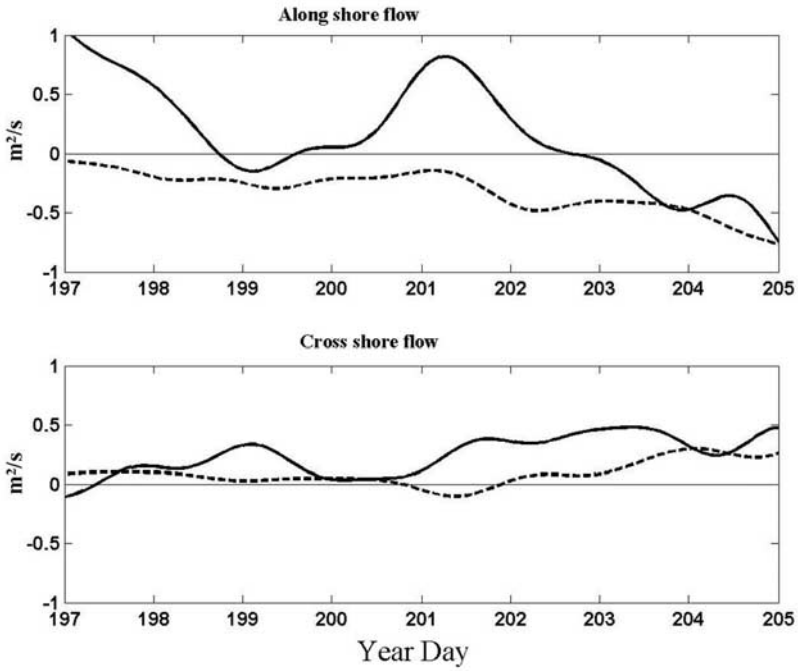

Figure 12. Upper and lower layer flow at LEO-15. (top) Along-shelf flow in upper layer (thick solid line) and lower layer (dashed line). (bottom) Cross-shelf flow in upper layer (thick solid line) and lower layer (dashed line).

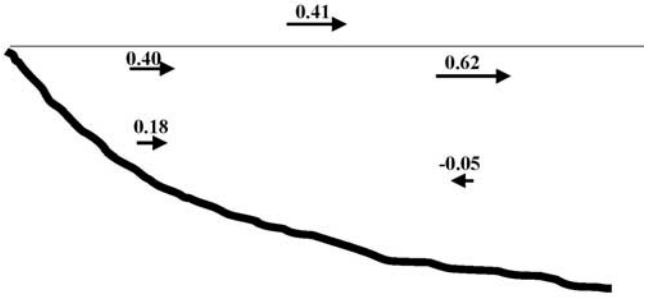

Figure 13. Schematic showing the mean cross-shelf transport per unit width (m^2/s) in upper and lower layer during the upwelling event. The mean cross-shelf transport predicted by Ekman's theory is shown above surface.

upwelling center is fed by the nearshore jet of cool water that veers offshore in the vicinity of LEO.

5. Discussion

[25] We have characterized the temporal evolution of a flow reversal during upwelling conditions and the subsequent development of an upwelling center in the vicinity of LEO-15. In particular, moored observations reveal that offshore transport in the surface mixed layer is initially consistent with an Ekman response to an alongshore wind stress. However, flow in the lower layer, while directed onshore, does not compensate for the offshore transport in the surface layer. This imbalance is evident at the daily timescale as well as at the event timescale (3–5 days) and is consistent with the findings of *Munchow and Chant* [2000], indicating that even on the seasonal timescales the mass balance is three-dimensional on this inner shelf.

[26] The mass balance at the event timescale is impacted by a nearshore flow reversal that veers offshore as it impinges on a shoaling and rougher topography. The evolution of the flow reversal was captured by towed ADCP data showing that it commenced during maximum alongshore wind stress and spins up in an inertial period. The flow reversal's structure is characterized by a jet where maximum velocities exceed 30 cm/s in the interior of the water column. The jet is 5 km wide and transports $\sim$20k m^3/s of thermocline fluid to the south. An additional 10k–25k m^3/s of down-shelf transport occurs offshore in the thermocline. As the jet spins up, the cross-shelf transport in the surface layer at the offshore mooring also increases. Prior to the flow reversal, off-shelf transport in the surface layer is consistent with Ekman transport, while following the flow reversal, offshore transport in the surface exceeds that predicted by Ekman's theory. Surface currents from CODAR indicate that the jet turns left and offshore as it impinges on the rougher topography at LEO-15. A similar veering of a coastal buoyant current has been observed at this location [*Yankovsky et al.*, 2000], and in the mean upwelling circulation pattern from CODAR [*Kohut et al.*, 2004].

[27] During this upwelling event, approximately 10 km^3 of fluid has been transported southward across the N-line and toward the upwelling center. This fluid tends to be a combination of thermocline water on the inshore side and colder lower layer water on the offshore side of the transect. This volume is approximately the volume of fluid contained in the southward drifting upwelling center observed with the AVHRR imagery on 23 July, assuming a mean water column depth of 15 m. Although upwelling is obviously associated with the onshore and upward movement of the western edge of the cold pool, we suggest that the down-shelf transport and offshore extension of the upwelling center is in part due to a convergence of the upwind nearshore jet as it veers offshore over the increasing rougher topography in the vicinity of LEO-15.

[28] Aspects of this structure are consistent with modeling results of *Song et al.* [2001]. Specifically, their results indicate that upwelled water is preferentially transported onshore downwind of a topographic high and forms a coastal current, opposed to the upwelling winds. This flow then turns offshore on the upwind side of the high where it competes with onshore flow in the bottom Ekman layer. On one hand, this is consistent with our observation of onshore flow in the bottom boundary layer that does not compensate the offshore flow in the surface layer. On the other hand, our observations indicate that the jet veers offshore upwind of the topographic high (Figure 6, top panel), and this differs from the *Song et al.* [2001] result that shows the nearshore return flow veering offshore south of the topographic high.

[29] The CTD sections indicate that the flow reversal is not associated with a buoyant current, and so the dynamics driving this differs from that described by *Yankovsky et al.* [2000] where fresh water from the Hudson's outflow impinged on the region. Rather we suggest that this flow reversal is driven by an adverse pressure gradient, similar to the modeling study by *Gan and Allen* [2002b], associated with flow curvature. Steerage of surface currents in this region by bottom topography is reported by *Kohut et al.* [2004] and apparent in surface current radar fields presented by *Chant* [2001]. Figure 14 presents idealized bottom topography used by *Song et al.* [2001] to depict topographic variability along the New Jersey shelf with a radius of curvature of 25 km. During the early phases of upwelling conditions, the up-shelf wind-driven flow meanders around these topographic features with a characteristic velocity of 0.15 cm/s [*Song et al.*, 2001; *Chant*, 2001; *Munchow and Chant*, 2000]. Assuming that the flow curvature (V^2/R) is balanced by a cross-shelf barotropic pressure gradient ($g\frac{\partial \eta}{\partial x}$) ($R$ = 25 km) results in a coastal setdown due to cylcostrophic forcing of approximately 0.4 cm at the topographic high and a coastal setup of the same magnitude where the flow curvature changes sign in the trough, 25 km to the north. Consequently, this would result in an alongshore sea surface slope of 0.8 cm/25 km = 3×10^{-7}. Note that while upwelling winds will drive a coastal setdown, it is the alongshore flow variability (i.e., flow curvature) that gives rise to the alongshore pressure gradients.

[30] An alongshore pressure gradient of a similar magnitude was revealed in EOF analysis of bottom pressure data collected here in 1996 [*Munchow and Chant*, 2000]. The first EOF mode, which contained nearly 95% of the variance, shows an alongshore barotropic pressure gradient that is enhanced on the shoreward side of the mooring array. During upwelling conditions the along-shelf pressure gra-

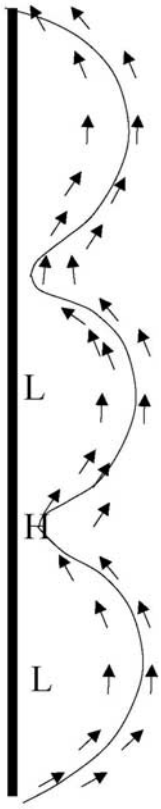

Figure 14. Schematic of flow bathymetry and flow curvature after *Song et al.* [2001].

dient is characterized by a sea level that slopes down-shelf 1.5 cm across the 40-km mooring array corresponding to a slope of approximately 4×10^{-7} and similar to the one inferred from the conceptual model (Figure 14).

[31] This estimate of the sea surface slope is of the right order to accelerate the flow reversal. Assuming an initial momentum balance between acceleration and the adverse pressure gradient, we can estimate that the down-shelf surface slope must be at least $\frac{\partial v}{\partial t} g^{-1}$, where v is the characteristic flow in the jet. The shipboard sections show that the flow reversal accelerates from rest to 20 cm/s in an inertial period (18.8 hours), and this requires a surface slope to the south of 3×10^{-7}, consistent with our other estimates of the adverse pressure gradient. Finally, after the jet has reached steady state, a balance between the pressure gradient and friction would yield a slope of $\frac{\tau_{by}}{gH} = \frac{C_d v^2}{gH}$, where H = 15 m, v is 0.20 m/s, and the bottom drag coefficient $C_d = 2 \times 10^{-3}$ yields a slope of 5.4×10^{-7}, again consistent in magnitude to the other estimates of the alongshore slope.

[32] What causes the jet to veer offshore and detach from the topography? Laboratory experiments by *Klinger* [1994] indicate that flow will separate from topography when the radius of curvature is less than v/f. However, during the event described in this paper, v/f is approximately 2000 m while the radius of curvature of the major bathymetric features are at least an order of magnitude larger. Yet other topographic scales are present. Specifically, a 5-km-scale ridge/swale topography with undulations spanning over 25% of the water column is superimposed on the topographic high (Figures 15a and 15b). One impact of the shoaling and rougher topography would be increased bottom friction due to wave-current interaction, because bottom wave orbital velocities will be larger over the rough topographic high south of LEO than orbital velocities north of LEO. In addition, large ripples form in response to the wave motion in these sandy sediments [*Traykovski et al.*, 1999].

[33] During this upwelling and relaxation event the period of surface gravity waves was typically 6 s, significant wave heights were 0.5–1 m, and bottom orbital velocities at LEO (12 m of water) were 20 cm/s (Figure 16). We estimate near-bottom wave orbital velocities on a transect north of LEO and transect south of LEO based on the dispersion relationship $\omega^2 = gk\tanh(kH)$, [*Leblond and Mysak*, 1978], where ω and k are the wave's frequency and wave number and g and H are gravity and water column depth. For 6-s waves the bottom orbital velocities ($\omega A/\sinh(kH)$ where A is the waves amplitude) are 50% higher and wave kinetic energy is twice as large on the southern line as on the northern line (Figures 15c and 15d). Furthermore, these increased near-bottom velocities would also be augmented by increased tidal currents near the coast in the vicinity of the inlet in contrast to the weaker tidal currents near the coast to the north (Figure 2).

[34] *Traykovski et al.* [1999] suggests that over 75% of the time, wave orbital velocities are large enough to initiate sediment motion and form wave orbital ripples at LEO. For 6- to 8-s-period waves [*Traykovski et al.*, 1999, Figure 18], initiation of sediment motion occurs with significant wave heights of 0.5–1 m. During the upwelling event described in this paper, wave conditions are near this transitional region and thus we expect ripples to form, particularly in the shoaling depths along the southern reaches of our study where wave orbital bottom velocities are larger. Furthermore, *Styles and Glenn* [2002] show that the largest ripples, often exceeding 10 cm, occur at this transitional point. From the law-of-the-wall scaling the coefficient of quadratic bottom drag $C_d = (\kappa/\ln(z/z_o))^2$ can be estimated. In the absence of sand ripples and wave-current interaction, typical z_o are less than 1 mm, while in the shallower depths the combination of ripple formation and a wave bottom boundary layer can produce an apparent z_o exceeding 20 cm [*Styles and Glenn*, 2002] corresponding to a factor of 10 increase in the bottom drag coefficient. In an environment where bottom drag is a dominant term in the momentum balance [*Lentz et al.*, 1999] an order of magnitude increase in the bottom drag coefficient must impact the flow structure. We suggest that increased drag will cause the flow to decelerate and drive the alongshore convergence characterized by the increased cross-shelf motion that we observe in the moored data.

[35] Form drag over the larger-amplitude ridge and swale topography would also augment bottom drag there. *MacCready and Pawlak* [2001] indicate that form drag over a single ridge can dominate the drag and drive an offshore transport. Since bottom friction is a first-order term in the along-shelf momentum balance on the inner shelf [*Lentz et al.*, 1999], a dramatic increase in drag over the rougher topography could reduce alongshore velocities and drive an offshore flow due to this convergence. This frictional increase in drag would be further aug-

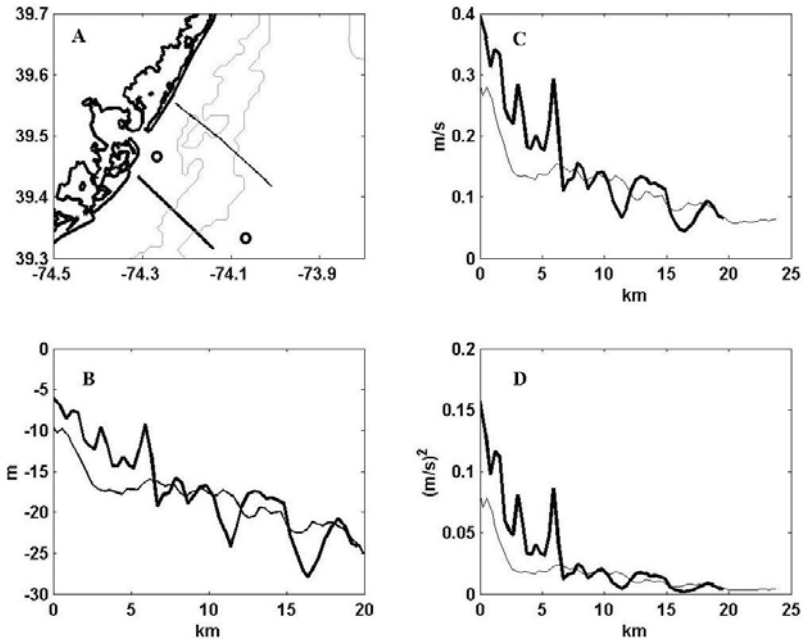

Figure 15. (a) Map showing cross-shelf sections used in ensuing three panels. In all figures, the thick line depicts the southern transect and the thin line depicts the northern transect. (b) Depth along transects shown in Figure 13 (top panel). (c) Wave orbital velocities at the bottom assuming a 6-s 1-m wave and a wave dispersion from *LeBlond and Mysak* [1978]. (d) Kinetic energy of wave orbital velocity.

mented by increased bottom friction associated with increased wave/current interaction and ripple formation over the ridges.

6. Conclusions

[36] With moored, shipboard, and remotely sensed data we have characterized the temporal evolution of a flow reversal during upwelling conditions and the subsequent development of an upwelling center on New Jersey's inner shelf. The flow reversal was initiated after a peak in upwelling-favorable winds and spins up in an inertial period. The flow reversal veers offshore as it impinges upon shoaling and rougher topography to the south and feeds a growing upwelling center. Moored data indicate that while offshore transport in the surface layer was initially

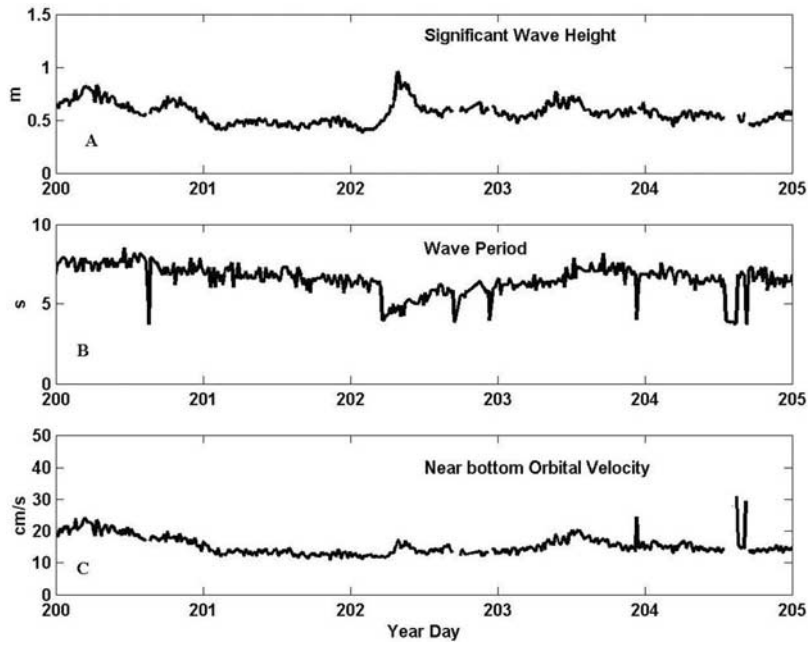

Figure 16. Wave parameters measured at LEO-15. (a) Significant wave height. (b) Peak wave period. (c) Bottom orbital wave velocity.

consistent with Ekman's theory, as the flow reversal spins up, the offshore transport in the surface layer exceeds the Ekman transport. The three dimensionality of the upwelling circulation is further emphasized by the fact that onshore flow in the bottom Ekman layer at the mooring site never compensates for the offshore transport in surface layer. The transport of fluid associated with the flow reversal is of the same order of magnitude as the volume of fluid in the evolving upwelling center, suggesting that the growth of the upwelling center is due to convergences in the alongshore flow rather than in the cross-shore flow. Estimates of alongshore pressure gradients required to maintain the flow curvature around the topography along the New Jersey shelf, as characterized by *Song et al.* [2001], are similar to those calculated in EOF analysis of bottom pressure records presented by *Munchow and Chant* [2000]. Furthermore, these estimates of the alongshore pressure gradient are consistent with both the pressure gradient required to spin up the flow reversal and maintain a steady flow when the pressure gradient is eventually balanced by friction. We further speculate that increased friction, due to both enhanced wave/current interactions and form drag, over shoaling and rougher topography causes the alongshore flow in the jet to converge and drive the flow offshore where it feeds a growing upwelling center. Insofar as the ridge and swale topography impacts the larger-scale dynamics, more detailed bathymetric data may be required to faithfully model this system.

[37] **Acknowledgments.** The authors acknowledge funding from the Office of Naval Research, the National Ocean Partnership Program (NOPP), and the Mid-Atlantic Bight National Undersea Research Center. Six of the current meter moorings used to generate the tidal model were deployed in 1996 as part of a National Science Foundation grant OCE-95-2839 of which Andreas Munchow, Rich Garvine, and Scott Glenn were the principal investigators. We thank Jennifer Bosch and Mike Crowley for the processing and plotting of AVHRR and CODAR data. We also thank two anonymous reviewers whose insights and comments have greatly improved this paper.

References

Austin, J. A., and J. A. Barth (2002), Variation in the position of the upwelling front on the Oregon shelf, *J. Geophys. Res.*, *107*(C11), 3180, doi:10.1029/2001JC000858.

Barth, J. A. (1994), Short wavelength instabilities on coastal jets and fronts, *J. Geophys. Res.*, *99*, 16,095–16,105.

Bernstein, R. L., L. Breaker, and R. Whitner (1977), California Current eddy formation, *Science*, *195*, 353–359.

Candela, J., R. C. Beardsley, and R. Limeburner (1992), Separation of tidal and subtidal currents in ship-mounted acoustic Doppler current profiler observations, *J. Geophys. Res.*, *97*, 769–788.

Chant, R. J. (2001), Evolution of near-inertial waves during an upwelling event on the New Jersey inner shelf, *J. Phys. Oceanogr.*, *31*, 746–764.

Chen, D., and D. P. Wang (1990), Simulating the time-variable coastal upwelling during CODE 2, *J. Mar. Res.*, *48*, 335–358.

Gan, J. P., and J. S. Allen (2002a), A modeling study of shelf circulation off northern California in the region of the Coastal Ocean Dynamics Experiment: 2: Simulations and comparisons with observations, *J. Geophys. Res.*, *107*(C11), 3184, doi:10.1029/2001JC001190.

Gan, J. P., and J. S. Allen (2002b), A modeling study of shelf circulation off northern California in the region of the Coastal Ocean Dynamics Experiment: Response to relaxation of upwelling favorable winds, *J. Geophys. Res.*, *107*(C9), 3123, doi:10.1029/2000JC000768.

Glenn, S. M., M. F. Crowley, D. B. Haidvogel, and T. S. Song (1996), Underwater observatory captures coastal upwelling events off New Jersey, *Eos Trans. AGU*, *77*, 233, 236.

Houghton, R. W., R. Schlitz, R. C. Beardsley, B. Butman, and J. L. Chamberlin (1982), The Middle Atlantic Bight cold pool: Evolution of the temperature structure during summer 1979, *J. Phys. Oceanogr.*, *12*, 1019–1029.

Huyer, A. (1983), Coastal upwelling in the California current system, *Prog. Oceanogr.*, *12*, 259–284.

Klinger, B. A. (1994), Inviscid current separation from rounded cape, *J. Phys. Oceanogr.*, *24*, 1805–1811.

Kohut, J. T., and S. M. Glenn (2003), Improving HF radar surface current measurements with measured antenna beam patterns, *J. Atmos. Oceanic Technol.*, *20*, 1303–1316.

Kohut, J. T., S. M. Glenn, and R. J. Chang (2004), Seasonal current variability on the New Jersey inner shelf, *J. Geophys. Res.*, *109*, C07S07, doi:10.1029/2003JC001963.

Kosro, P. M. (1987), Structure of the coastal current field off northern California during the Coastal Ocean Dynamics Experiment, *J. Geophys. Res.*, *92*, 1637–1654.

Large, W. G., and S. Pond (1981), Open ocean momentum flux measurements in moderate to strong winds, *J. Phys. Oceanogr.*, *11*, 324–336.

LeBlond, P. H., and L. A. Mysak (1978), *Waves in the Ocean*, 602 pp., Elsevier Sci., New York.

Lentz, S. J., and J. H. Trowbridge (1991), The bottom boundary layer over the northern California shelf, *J. Phys. Oceanogr.*, *21*, 1186–1201.

Lentz, S., R. T. Guza, S. Elgar, F. Feddersen, and T. H. C. Herbers (1999), Momentum balances on the North Carolina inner shelf, *J. Geophys. Res.*, *104*, 18,205–18,226.

MacCready, P., and G. Pawlak (2001), Stratified flow along a corrugated slope: Separation drag and wave drag, *J. Phys. Oceanogr.*, *31*, 2824–2839.

MacCready, P., and P. B. Rhines (1993), Slippery bottom boundary layers on a slope, *J. Phys. Oceanogr.*, *23*, 5–22.

Munchow, A., and R. J. Chant (2000), Kinematics of inner shelf motion during the summer stratified season off New Jersey, *J. Phys. Oceanogr.*, *30*, 247–268.

Send, U., R. C. Beardsley, and C. D. E. Winant (1987), Relaxation from upwelling in the coastal ocean dynamics experiment, *J. Geophys. Res.*, *92*, 1683–1698.

Signell, R. P., and W. R. Geyer (1991), Transient eddy formation around headlands, *J. Geophys. Res.*, *96*, 2561–2575.

Smith, R. L. (1981), A comparison of the structure and variability of the flow field in three coastal upwelling regions: Oregon, northwest Africa, and Peru, in *Coastal Upwelling*, *Coastal Estuarine Stud.*, vol. 1, edited by F. A. Richards, pp. 108–118, AGU, Washington, D. C.

Song, Y. T., D. B. Haidvogel, and S. M. Glenn (2001), Effects of topographic variability on the formation of upwelling centers off New Jersey: A theoretical model, *J. Geophys. Res.*, *106*, 9223–9240.

Styles, R., and S. M. Glenn (2002), Modeling bottom roughness in the presence of wave-generated ripples, *J. Geophys. Res.*, *107*(C8), 3110, doi:10.1029/2001JC000864.

Traganza, E. C., J. C. Conrad, and L. C. Breaker (1981), Satellite observations of a cyclonic upwelling system and giant plume in the California Current, in *Coastal Upwelling*, *Coastal Estuarine Stud.*, vol. 1, edited by F. A. Richards, pp. 228–241, AGU, Washington, D. C.

Traykovski, P., A. E. Hay, J. D. Irish, and J. F. Lynch (1999), Geometry, migration and evolution of wave orbital ripples at LEO-15, *J. Geophys. Res.*, *104*, 1505–1524.

Trowbridge, J. H., and S. J. Lentz (1991), Asymmetric behavior of an oceanic boundary layer over a sloping bottom, *J. Phys. Oceanogr.*, *21*, 1171–1185.

Wang, D. P. (1997), Effects of small-scale wind on coastal upwelling with application to Point Conception, *J. Geophys. Res.*, *102*, 15,555–15,570.

Winant, C. D., R. C. Beardsley, and R. E. Davis (1987), Moored wind, temperature and current observations made during Coastal Ocean Dynamics Experiments 1 and 2 over the northern California continental shelf and upper slope, *J. Geophys Res.*, *92*, 1569–1604.

Yankovsky, A. E., R. W. Garvine, and A. Munchow (2000), Mesoscale currents on the inner New Jersey shelf driven by the interaction of buoyancy and wind forcing, *J. Phys. Oceanogr.*, *30*, 2214–2230.

R. J. Chant, S. Glenn, and J. Kohut, Institute of Marine and Coastal Science, Rutgers University, 74 Dudley Road, New Brunswick, NJ 08901, USA. (chant@imcs.rutgers.edu)